A&A, 690, A128 (2024)
https://doi.org/10.1051/0004-6361/202451778

Astronomy & Astrophysics

The solar beryllium abundance revisited with 3D non-LTE models

A. M. Amarsi[1,⋆], D. Ogneva[1], G. Buldgen[2], N. Grevesse[2,3], Y. Zhou[4], and P. S. Barklem[1]

[1] Theoretical Astrophysics, Department of Physics and Astronomy, Uppsala University, Box 516, SE-751 20 Uppsala, Sweden
[2] Space sciences, Technologies and Astrophysics Research (STAR) Institute, Université de Liège, Allée du 6 août, 17, B5C, B-4000 Liège, Belgium
[3] Centre Spatial de Liège, Université de Liège, avenue Pré Aily, B-4031 Angleur-Liège, Belgium
[4] School of Physical and Chemical Sciences – Te Kura Matū, University of Canterbury, Private Bag 4800, Christchurch 8140, Aotearoa, New Zealand

Received 2 August 2024 / Accepted 22 August 2024

ABSTRACT

The present-day abundance of beryllium in the solar atmosphere provides clues about mixing mechanisms within stellar interiors. However, abundance determinations based on the Be II 313.107 nm line are prone to systematic errors due to imperfect model spectra. These errors arise from missing continuous opacity in the UV, a significant unidentified blend at 313.102 nm, departures from local thermodynamic equilibrium (LTE), and microturbulence and macroturbulence fudge parameters associated with one-dimensional (1D) hydrostatic model atmospheres. Although these factors have been discussed in the literature, no study has yet accounted for all of them simultaneously. To address this, we present 3D non-LTE calculations for neutral and ionised beryllium in the Sun. We used these models to derive the present-day solar beryllium abundance, calibrating the missing opacity on high resolution solar irradiance data and the unidentified blend on the centre-to-limb variation. We find a surface abundance of 1.21 ± 0.05 dex, which is significantly lower than the value of 1.38 dex that has been commonly adopted since 2004. Taking the initial abundance via CI chondrites, our result implies that beryllium has been depleted from the surface by an extra 0.11 ± 0.06 dex, or 22 ± 11%, on top of any effects of atomic diffusion. This is in tension with standard solar models, which predict negligible depletion, as well as with contemporary solar models that have extra mixing calibrated on the abundances of helium and lithium, which predict excessive depletion. These discrepancies highlight the need for further improvements to the physics in solar and stellar models.

Key words. atomic processes – line: formation – radiative transfer – Sun: abundances – Sun: evolution – Sun: photosphere

1. Introduction

Beryllium is an interesting tracer of the structure and evolution of the Sun and other late-type stars. ^{9}Be is destroyed at temperatures of around 3.5×10^6 K, that is, at temperatures slightly greater than that of ^{7}Li (2.5×10^6 K; e.g. Lamia et al. 2015). Given that the temperature at the base of the solar convective zone ranges from around 2.45×10^6 K to 2.20×10^6 K from birth until today (e.g. Christensen-Dalsgaard 2021), the depletion of beryllium in the solar atmosphere, and the relative depletion of beryllium compared to lithium, can help constrain the mixing of material from the convective envelope into the radiative interior (e.g. Eggenberger et al. 2022; Buldgen et al. 2023).

The total cumulative depletion of beryllium in the Sun is determined by the difference between the initial abundance and the current surface abundance. The initial abundance is typically assumed to be well-represented by CI chondrites (e.g. Suess & Urey 1956; Anders & Grevesse 1989; Lodders et al. 2009). Although there are hints of trends in CI chondrite compositions with condensation temperature (Gonzalez 1997; Gonzalez et al. 2010; Asplund et al. 2021); the effect of this is minimised by using an abundant species of similar condensation temperature to beryllium (T_c = 1551 K; Wood et al. 2019) to convert from the meteoritic scale to the solar scale[1]. Using silicon (T_c = 1314 K), magnesium (T_c = 1343 K), or iron (T_c = 1338 K), with A(Si) = 7.51 ± 0.03, A(Mg) = 7.55 ± 0.03, or A(Fe) = 7.46 ± 0.04 (Asplund et al. 2021), the CI chondrite abundances from Lodders (2021) are $A(\mathrm{Be})_{\mathrm{init}}$ = 1.31 ± 0.05, 1.34±0.05, and 1.32±0.05, respectively, for the initial solar composition[2]. Taking the mean, we arrive at $A(\mathrm{Be})_{\mathrm{init}}$ = 1.32 ± 0.04.

The current surface abundance of beryllium must be determined from analysing the solar spectrum. The Be II 313 nm resonance doublet is the most useful feature in the spectra of late-type stars (e.g. Boesgaard 2023; Smiljanic et al. 2023). In the Sun, the stronger component at 313.042 nm (in air) is heavily affected by blends. For the weaker component at 313.107 nm, the focus of this study, precise and accurate determinations of the solar beryllium abundance is hindered by four uncertainties of potentially comparable importance: a) missing continuous opacity; b) a significant blend at around 313.102 nm; c) errors caused by the assumption of local thermodynamic equilibrium (LTE); and d) errors caused by the use of one-dimensional (1D) model atmospheres.

So far, there have not been any studies of the solar beryllium abundance to address all four uncertainties simultaneously. A notable work is that of Chmielewski et al. (1975). They accounted for missing continuous opacity by considering the continuous centre-to-limb variation, and they accounted for the blend by considering the shape of the Be II 313.107 nm line

⋆ Corresponding author; anish.amarsi@physics.uu.se

[1] This protosolar abundance may be slightly higher because this conversion erases the effects of atomic diffusion (microscopic thermal diffusion, gravitational settling, and radiative acceleration), given that they are predicted to be of a similar magnitude for all elements heavier than helium (see Section 5 of Asplund et al. 2021).

[2] $A(\mathrm{X}) \equiv \log_{10} N_{\mathrm{X}}/N_{\mathrm{H}} + 12$.

at disc-centre ($\mu = 1.0$) and at the limb ($\mu = 0.2$). In this way they found that the blend constitutes almost half of the equivalent width at the limb (see their Figure 6). They carried out non-LTE calculations with a small nine-level model atom for neutral and ionised beryllium using a revised version of the 1D semi-empirical model atmosphere of Holweger & Müller (1974). They ultimately arrived at A(Be) = 1.15±0.20. The mean value implies a depletion of around 30%, although the large error bar makes it consistent with no depletion to one standard error.

The later work by Balachandran & Bell (1998) took a different approach to calibrating for any missing continuous opacity: namely, they considered A-X electronic transitions of OH close to the Be II doublet, and demanded that they yield the same oxygen abundance as vibrational-rotational transitions in the infrared. Their subsequent analysis was based solely on disc-integrated flux (rather than the centre-to-limb variation as in Chmielewski et al. 1975) and they did not discuss the impact of the blend. They also did not discuss departures from LTE, and they used the 1D semi-empirical atmosphere of Holweger & Müller (1974). In all they obtained A(Be) = 1.40 ± 0.09, consistent with no depletion of beryllium in the Sun.

Asplund (2004) presented a reanalysis of Balachandran & Bell (1998). The primary development was the use of a 3D hydrodynamical model atmosphere, both for calibrating the missing continuous opacity via OH lines, and for determining the beryllium abundances. Asplund (2004) arrived at A(Be) = 1.38 ± 0.09: again, consistent with no depletion of beryllium in the solar convective envelope. This value is also given in the compilation of Asplund et al. (2021), although it is cautioned that this value is likely to be overestimated owing to the limitations in the original studies of Balachandran & Bell (1998) and Asplund (2004): in particular, they neglected the impact of the blend as well as departures from LTE.

In a more recent study, Carlberg et al. (2018) analyse the disc-integrated flux from the Sun observed from the asteroid Vesta, as well as spectra from the red giants Arcturus and Pollux. They updated a line list around the Be II 313 nm lines from Delgado Mena et al. (2012) and Takeda et al. (2011) (the latter originally developed by Primas et al. 1997) to fit these three spectra using a theoretical `MARCS` 1D model atmosphere (Gustafsson et al. 2008), and 1D LTE spectrum synthesis. In doing so they argue that the unidentified blend is probably due to an ionised species, and is of low excitation potential – just as Chmielewski et al. (1975) argued on the basis of the solar centre-to-limb variation. Using their calibrated line list, they derived a solar abundance of A(Be) = 1.30, consistent with no depletion of beryllium. Nonetheless they cautioned of large systematic uncertainties, largely stemming from the calibration of the missing continuous opacity via an OH line.

A very recent work on this topic is that of Korotin & Kučinskas (2022). Their analysis, like that of Balachandran & Bell (1998) and Asplund (2004), was based on the disc-integrated flux. The missing continuous opacity was calibrated by comparing against the observed low-resolution absolute disc-integrated flux in the near-UV region. Rather than adding hypothetical lines, the authors start with a predicted line list from the VALD database (e.g. Heiter et al. 2008), and modified the oscillator strengths and wavelengths of blending lines mainly on the basis of literature recommendations (which in turn are based on 1D LTE analyses of the Sun and other stars). In particular, the unidentified blend was taken to be the known Mn I 313.104 nm line, with its oscillator strength and wavelength adjusted to the values given by Ashwell et al. (2005). With this line list, the authors presented a non-LTE analysis of neutral and ionised beryllium based on an extensive model atom with up-to-date collisional data. They arrived at A(Be) = 1.32 ± 0.05 and A(Be) = 1.35 ± 0.05, using a theoretical `ATLAS9` 1D model atmosphere (Castelli et al. 2003) and the 1D semi-empirical model atmosphere of Holweger & Müller (1974), respectively. Again, there is no indication of significant depletion of beryllium in the solar atmosphere.

Here, we revisit the solar beryllium abundance. We attempted to take into account all of the problems mentioned above in a single study: namely, the missing continuous opacity, and the 313.102 nm blend, together with 3D non-LTE effects. We first present an overview of the 3D non-LTE calculations in Section 2, before presenting our analysis of the solar beryllium abundance in Section 3. We ultimately found evidence of some beryllium depletion in the solar envelope; we discuss the implications of this result on the structure and evolution of the Sun in Section 4, and then summarise our findings in Section 5.

2. Models

2.1. Model solar atmospheres

The post-processing radiative transfer calculations presented in this work were performed on a 3D radiation-hydrodynamics simulation of the solar surface carried out with the `Stagger` code (Collet et al. 2011; Magic et al. 2013). This model atmosphere was first used and discussed in Amarsi et al. (2018a), and has been employed in several follow-up studies (Amarsi et al. 2019, 2020; Asplund et al. 2021); in particular, it was used in the analysis of molecular lines of carbon, nitrogen, and oxygen presented in Amarsi et al. (2021). It was constructed assuming the solar composition presented in Asplund et al. (2009). The mean effective temperature of the model is 5773 K, with a snapshot-to-snapshot standard deviation of 16 K.

Radiative transfer calculations were also performed on the theoretical `MARCS` 1D model of the solar atmosphere (Gustafsson et al. 2008). These calculations were only used to quantify the 3D versus 1D effects, as well as to help elucidate the physical mechanisms of the departures from LTE, as we discuss in Section 2.4.

2.2. Spectrum synthesis

Two codes were used for the post-processing radiative transfer calculations: the 3D LTE code `Scate` (Hayek et al. 2011), and the 3D non-LTE code `Balder` (Amarsi et al. 2018b). The latter code is based on `Multi3D` (Leenaarts & Carlsson 2009), with updates including to the equation of state and opacities (e.g. Amarsi et al. 2016; Zhou et al. 2023).

The `Scate` calculations were performed on ten snapshots of the solar model: this is the number of snapshots recommended by Rodríguez Díaz et al. (2024) for reliable time-averaged spectral line profiles. These calculations include the Be II line, as well as 74 known blending lines plus one hypothetical line, as we discuss in Section 3.2. The abundances of background species were for the most part set to those given in Asplund et al. (2021). The exceptions are for carbon, nitrogen, and oxygen: as molecules of CN and OH are present in the Be II 313.107 nm region, the abundances of these elements were set to those derived from a 3D LTE analysis of molecular lines given in Amarsi et al. (2021). The spectra were calculated at disc-centre $\mu = 1.0$ and at the limb $\mu = 0.2$: the latter, via integration in the azimuthal angle ϕ using the 8-point trapezoidal quadrature. The disc-integrated fluxes were calculated using the 4-point Gauss quadrature for

the μ integration and the 4-point trapezoidal quadrature for the ϕ integration on the unit hemisphere.

As we discuss in Section 3, the analysis had several free parameters including the beryllium abundance, the oscillator strength and the wavelength of the hypothetical line that blends the Be II 313.107 nm feature, and a scale factor for the missing continuous opacity. As such `Scate` calculations were performed to generate a rectilinear grid of spectra, with each of these parameters taking a range of values. The beryllium abundance and the oscillator strength of the blend were varied in steps of 0.2 dex, the wavelength of the blend was varied in steps of 0.0005 nm, and the missing continuous opacity factor was varied in steps of 0.25.

The 3D non-LTE spectra were constructed by calculating 3D non-LTE to 3D LTE ratios for the Be II line using `Balder` on eight snapshots of the same solar model, and applying them to the blended 3D LTE spectrum calculated using `Scate` as described above. These 3D non-LTE calculations were carried out in an analogous way to previous works on the Sun (e.g. Amarsi et al. 2018a, 2019, 2020). In particular, the mean radiation field J_ν was calculated using 26 rays on the unit sphere (13 outgoing, and 13 ingoing), including the two vertical rays, using the 8-point Lobatto quadrature for the μ integration and the 4-point trapezoidal quadrature for the ϕ integration. The statistical equilibrium calculations were performed using the reduced model atom that we discuss in Section 2.3. Although background line opacities were included in the calculation of the statistical equilibrium, the final line profiles that were used for the 3D non-LTE to 3D LTE ratios were calculated without any blends. The emergent intensities were calculated using the 10-point Lobato quadrature for the μ integration and the 8-point trapezoidal quadrature for the ϕ integration on the unit hemisphere. The vertical was explicitly included in this set, but the rays at $\mu = 0.2$ are not. Consequently the 3D non-LTE to 3D LTE ratios at the limb were found by cubic spline interpolation in μ. As with the `Scate` calculations, spectra were calculated for a range of beryllium abundances in steps of 0.2 dex. In terms of equivalent width, the 3D LTE profiles for the Be II 313.107 nm line alone calculated by `Scate` and `Balder` with the adopted setup were found to agree to better than 0.005 dex for the disc-centre intensity and disc-integrated flux, and 0.018 dex for the intensity at $\mu = 0.2$. The larger difference at the limb is mainly due to the different treatment of UV continuous opacity between the two codes, which to first order cancels out in the 3D non-LTE to 3D LTE ratios used here.

Solely for the purpose of discussing 3D and non-LTE effects (Section 2.4), calculations were also performed on 1D model atmospheres (see Section 2.1). `Scate` and `Balder` were also used for these calculations, in a similar way as for the 3D calculations. The main difference here is that a depth-independent microturbulence of 1.0 km s^{-1} was assumed. No such microturbulence was adopted for the 3D calculations, since these broadening effects are naturally accounted for in the 3D radiative transfer calculations. The discussion in Section 2.4 is based on equivalent widths, and therefore macroturbulence (another free parameter in commonly used in analyses based on 1D models) is not relevant here.

2.3. Model atom

A comprehensive model atom was constructed for this work, for the most part following the steps described in Section 2.2 of Korotin & Kučinskas (2022). The most significant difference is that, here, fine structure is taken into account for the Be II 313 nm lines in the calculation of J_ν and subsequently when evaluating the radiative rates. In addition, recent data for inelastic collisions between ionised beryllium and electrons from Dipti et al. (2024) are included in this work. The complexity of this comprehensive model was then reduced, to make it feasible to run the 3D non-LTE calculations. Early versions of these atoms are described in more detail in Ogneva (2023).

We illustrate the grotrian diagram of the comprehensive model in the left panels of Figure 1. This comprehensive model contains 236 energy levels: 181 are of neutral beryllium, 54 are of ionised beryllium, and the ground state of doubly ionised beryllium is also included. The data come from the Atomic Spectra Database of the National Institute of Standards and Technology (NIST ADS; Ralchenko & Kramida 2020) with fine structure collapsed; and from the Opacity Project Atomic Databse (TOPBase; Cunto et al. 1993). These included levels reaching 0.14 eV below the ionisation limit for neutral beryllium, and 0.55 eV below the ionisation limit for ionised beryllium. Rydberg levels missing in these data set were then introduced, assuming them to be hydrogen-like; however, unlike the other levels, these were only allowed to couple collisionally to the other levels in the model atom.

The photoionisation cross-sections as well as most of the bound-bound transition data originated from TOPBase. The natural broadening parameters were calculated from the TOPBase data, and broadening due to elastic collisions with neutral hydrogen were calculated with the commonly used Lindholm-Foley-Unsöld theory (LFU, Unsöld 1955; see also Barklem 2016a), with an enhancement factor of two. The UV lines of Be I as well as the Be II 313 nm lines themselves strongly impact the statistical equilibrium and were given special treatment: the TOPBase oscillator strengths were replaced with those from NIST ASD (originating from Tachiev & Froese Fischer 1999 and related calculations). Moreover, the hydrogen broadening for these lines were calculated using ABO theory (Anstee & O'Mara 1995; Barklem & O'Mara 1997; Barklem et al. 1998; Barklem & O'Mara 2000), taking the parameters listed in VALD. In addition, fine structure was taken into account for these lines in the calculation of J_ν and subsequently when evaluating the radiative rates and solving for the statistical equilibrium. At least in this case (for the Sun), the effect of splitting the Be II 313 nm lines in this way has a subtle impact on the equivalent widths, with a corresponding significant effect on the abundance corrections because the lines are saturated, as we discuss in Section 2.4.1; whereas accounting for fine structure of the Be I lines did not make a significant impact on the overall results.

The cross-sections for inelastic collisions with electrons (excitation and ionisation) involving the important low-lying levels of neutral and ionised beryllium were taken from Dipti et al. (2019) and Dipti et al. (2024). These data are primarily based on the convergent close-coupling method (CCC; Bray & Stelbovics 1992); for neutral beryllium data based on the B-Spline R-matrix method (BSR; Zatsarinny 2006). These data were supplemented with data from the ADAS project (Summers & O'Mullane 2011). For highly excited levels the inelastic electron collisions were described with the recipes of van Regemorter (1962) and Allen (1973); these are of lower accuracy, but through 1D non-LTE calculations we verified that switching them off had no impact on the strength of the Be II 313.107 nm line.

For inelastic collisions with neutral hydrogen (excitation and charge transfer), the low-lying levels of neutral beryllium were described using the data given in Yakovleva et al. (2016). These are based on an asymptotic model for the potentials com-

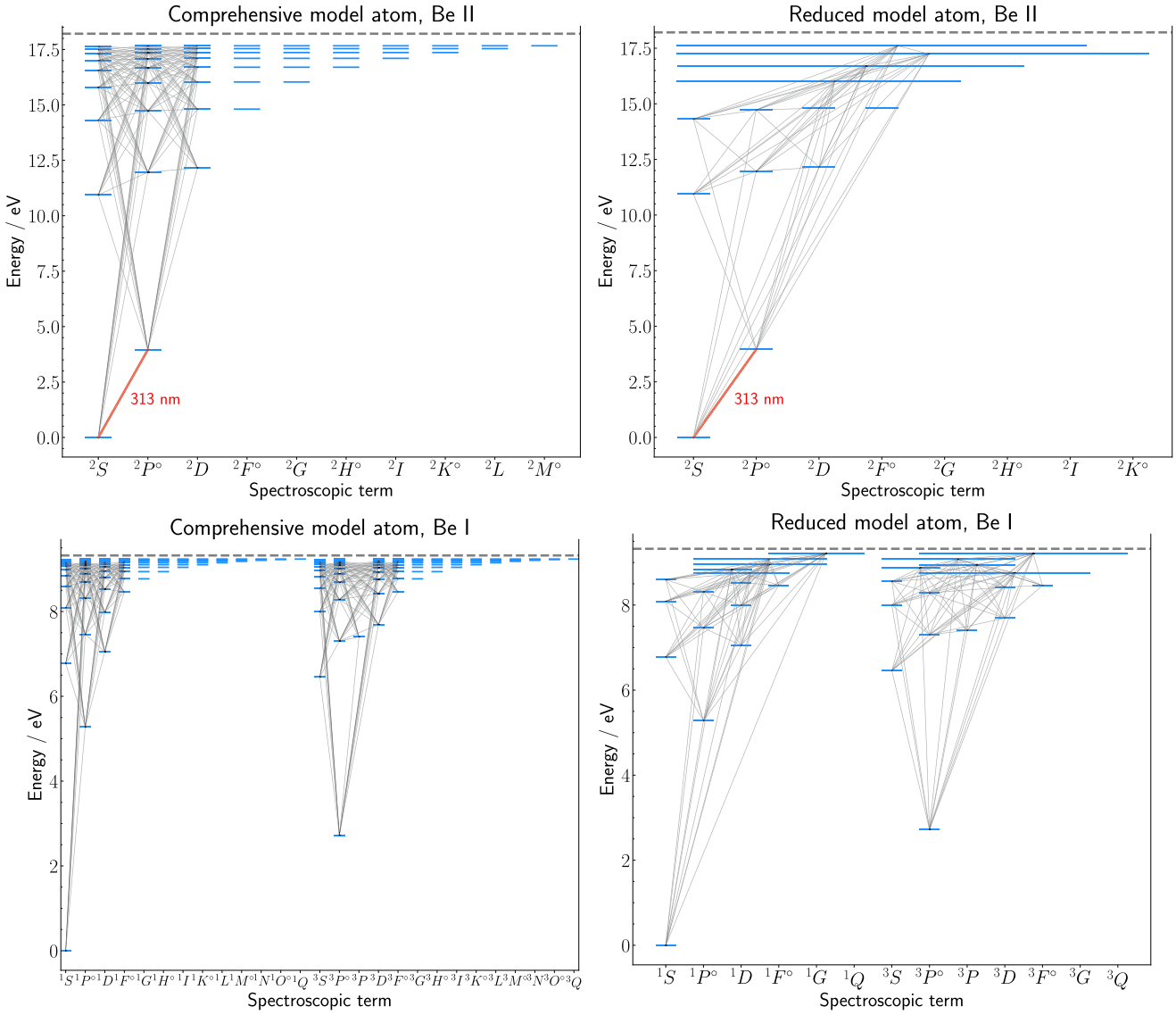

Fig. 1. Grotrian diagrams of singly ionised (upper panels) and neutral (lower panels) beryllium as represented in the comprehensive (left panels) and reduced (right panels) model atoms used in this work.

bined with the Landau-Zener approach for the collision dynamics (e.g. Belyaev 2013; Barklem 2016b). Data calculated using the free electron approach of Kaulakys (1985, 1986, 1991), in the scattering-length regime, were added to this as motivated in Amarsi et al. (2018a, 2019), and also discussed further in Schmidt-May et al. (2024). For ionised beryllium, excitation and ionisation by impact with neutral hydrogen were described using the Drawin recipe (as described in Appendix A of Lambert 1993), without any scaling. Similarly to the tests on the electron rates, we verified that switching off the free electron rates and the Drawin rates did not impact the Be II 313.107 nm line in 1D non-LTE.

A reduced model atom was constructed from this comprehensive one in order to make the 3D non-LTE radiative transfer calculations feasible (e.g. Section 2.2.4 of Lind & Amarsi 2024). Levels above $1s2.2s.5s\,{}^1S$ of neutral beryllium and $1s2.4f^2\,F^o$ of ionised beryllium were collapsed into ten and four super levels, respectively. The radiative and collisional transitions involving these were similarly collapsed into super transitions. We illustrate the grotrian diagram of this reduced model in the right panels of Figure 1. Once again, we verified in 1D non-LTE that this reduction had a negligible impact on the Be II 313.107 nm: at most 0.00014 dex in terms of abundance corrections, with the effects largest at the solar limb.

2.4. 3D non-LTE effects

We illustrate the 1D non-LTE, 3D LTE, and 3D non-LTE effects on abundances inferred from the Be II 313.107 nm line in Figure 2. The panels illustrate various types of abundance corrections based on equivalent widths, calculated at a given reference abundance. For example, a positive value of the 3D non-LTE versus 1D LTE abundance correction indicates that the reference abundance inferred from a 1D LTE analysis of equivalent widths underestimates the beryllium abundance compared to a 3D non-LTE analysis; the 1D LTE lines in that case are too strong at given abundance. The left panel shows the abundance corrections as a function of μ for a fixed reference beryllium abundance $A(\mathrm{Be}) = 1.18$, while the right panel shows the abundance corrections as a function of $A(\mathrm{Be})$, at disc-centre and at the limb.

All of the abundance corrections in the intensities shown in the left panel of Figure 2 change sign when going from

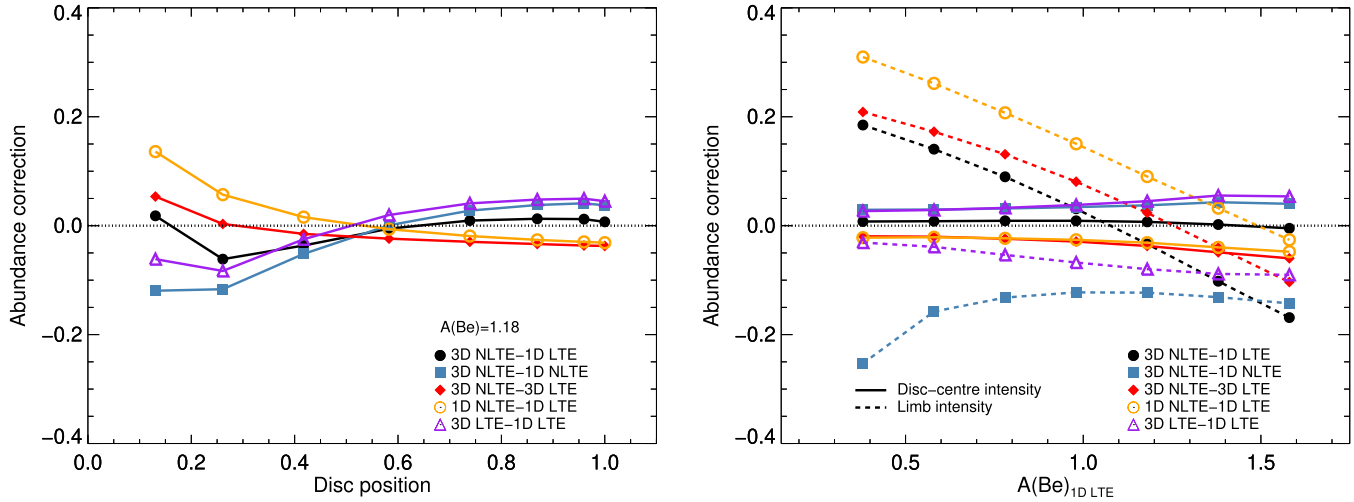

Fig. 2. Abundance corrections for the Be II 313.107 nm, based on equivalent widths as a function of μ at a reference abundance of A(Be) = 1.18 (left panel), and of A(Be) for the disc-centre (μ = 1.0) and limb (μ = 0.2) intensities (right panel). The 1D calculations adopt a fixed microturbulence of 1 km s^{-1}.

disc-centre to the limb. A consequence of this is that the corresponding abundance corrections for the disc-integrated flux are close to zero. The non-LTE effect on the disc-integrated flux (3D non-LTE versus 3D LTE abundance correction) amounts to −0.027 dex, while the 3D effect (3D non-LTE versus 1D non-LTE abundance correction) amounts to +0.015 dex. The 1D non-LTE versus 1D LTE abundance correction is −0.014 dex and consequently the 3D non-LTE versus 1D LTE abundance correction is close to zero, at this abundance. The 3D LTE versus 1D LTE abundance correction is somewhat larger than the 3D non-LTE versus 1D non-LTE one: +0.031 dex.

2.4.1. Non-LTE effects

In order to gain a qualitative understanding of the main non-LTE mechanism, it is helpful to look at the departure coefficients. Figure 3 shows that, for most levels (including the lower and upper level of the Be II 313 lines), the departure coefficients predicted by the 1D non-LTE calculations roughly follow the distribution of departure coefficients predicted by the 3D non-LTE calculations. As such, we have used 1D non-LTE calculations to study and understand the departures from LTE. Quantitatively, the 3D non-LTE versus 3D LTE abundance corrections are indeed similar to the 1D non-LTE versus 1D LTE abundance corrections at disc-centre (Figure 2); the two quantities drift apart from each other towards the limb, with more severe positive non-LTE corrections in the 3D model.

In the current model, the main non-LTE effects relevant to the Be II 313 nm lines are caused by photon pumping of bound-bound transitions in the UV. We illustrate this in Figure 4, using the results of 1D non-LTE test calculations. There are two competing photon pumping effects. First, pumping of the Be I lines in the UV leads to an overpopulation of the excited levels of neutral beryllium. This excess population flows into the ground state of ionised beryllium via collisions. This increase in population leads to strengthening of the Be II 313 nm lines, an effect that corresponds to negative abundance corrections relative to LTE. Secondly, and in competition, pumping of the Be II 313 nm lines themselves tends to increase the population of the upper level and reduce the population of the lower level. This weakens the lines, corresponding to positive abundance corrections relative to LTE. In Figure 4 it can be seen that switching the Be I UV lines off sets the departure coefficients of the lower level of the Be II 313 nm lines (the ground state of ionised beryllium) to be close to unity (upper left panel of Figure 4); and further switching off the Be II 313 nm lines themselves then also sets the departure coefficients of the upper level to be close to unity (upper right panel of Figure 4); the emergent line profiles in that case then do not display any deviations from LTE (lower right panel of Figure 4).

This picture is qualitatively similar to that presented in Section 3.4 of Garcia Lopez et al. (1995). The main difference is that those authors find a significant pumping of the Be I photoionisation processes themselves; here, it is rather the pumping of the Be I lines that are driving the effects. Quantitatively, the 1D non-LTE versus 1D LTE abundance corrections for the disc-integrated flux (−0.014 dex as we discussed above) are similar to those given by Garcia Lopez et al. (1995) and Takeda et al. (2011). Korotin & Kučinskas (2022) report a more severe correction of −0.07 dex. As we illustrate in Figure 4, this is possibly due to their neglecting fine structure of the Be II 313 nm lines in their statistical equilibrium calculations (when calculating J_ν and subsequently evaluating the radiative rates). Merging the lines reduces the photoexcitation rates in the transition (see the discussion in Appendix B of Steffen et al. 2015). Thus by doing so the second non-LTE effect described above (pumping of the Be II 313 nm lines themselves, which weakens the lines and leads to positive 1D non-LTE abundance corrections) is reduced and the lines get stronger overall ("No Be II 313 nm F-S" in the lower right panel of Figure 4). In this model, assuming A(Be) = 1.18, the equivalent width then increases such that the 1D non-LTE versus 1D LTE abundance correction becomes −0.07 dex, in excellent agreement with Korotin & Kučinskas (2022).

The competition between the two non-LTE effects helps explain the behaviour of the 3D non-LTE versus 3D LTE abundance corrections with disc position and with 3D LTE beryllium abundance seen in Figure 2 (red diamonds). These abundance corrections are negative at disc-centre, suggesting that photon pumping of the Be I UV lines is more important there. At the limb, the 3D non-LTE versus 3D LTE abundance corrections are positive, suggesting that instead photon pumping of the Be II 313 nm lines themselves increasingly dominate at higher layers in the atmosphere. This is consistent with the run of the ratio of departure coefficients of the upper and lower levels

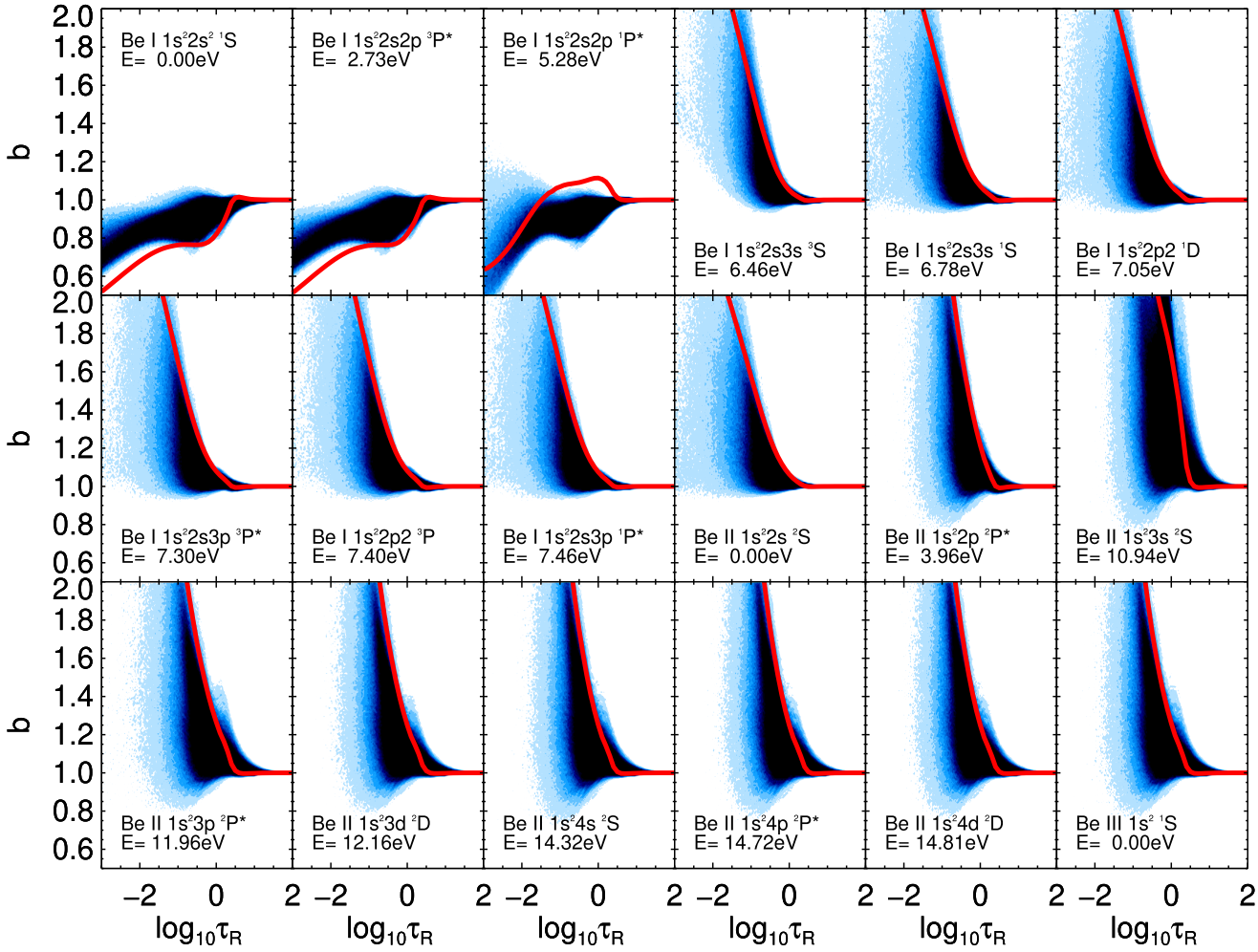

Fig. 3. Departure coefficients for the lowest levels of neutral and ionised beryllium, and for the ground state of doubly ionised beryllium, as a function of the logarithmic Rosseland mean optical depth. Contours show the distribution of results from the 3D calculations; the thick red line shows the results from the 1D calculations. These calculations adopt A(Be) = 1.18.

(lower left panel of Figure 4): this ratio increases towards higher layers, indicating an increasing line source function relative to LTE and therefore more weakening relative to LTE. At the limb, the 3D non-LTE versus 3D LTE abundance corrections show a strong sensitivity to the beryllium abundance, becoming more negative with increasing A(Be). Increasing the beryllium abundance increases the strength of the Be II 313 nm lines, up to and beyond saturation; this in turn increases the photon losses in the line (which is efficient for saturated lines), which counteracts the photon-pumping effect described above.

2.4.2. 3D effects and their coupling with the non-LTE effects

The 3D effects on the Be II 313 nm lines are here quantified by the 3D non-LTE versus 1D non-LTE abundance corrections. These are slightly positive at disc-centre (blue squares in Figure 2). This is consistent with findings for other saturated resonance lines of majority species, as seen in Figure 6 of Lind & Amarsi (2024), where the effects are separated into that caused by differences in the mean stratification and that caused by inhomogeneities resulting from solar granulation. According to that plot, the effect of the mean stratification dominates: the 3D model has a slightly shallower temperature gradient, which weakens the lines compared to those generated from the 1D model.

At the limb, the 3D non-LTE versus 1D non-LTE abundance corrections change sign, becoming negative and more severe: the 3D non-LTE line is much stronger than the 1D non-LTE one, at given 1D non-LTE abundance. When observing the limb, the granules are seen edge-on. The horizontal velocity fields being larger than the vertical velocity fields in the 3D models (e.g. Stein & Nordlund 1998, Figure 5), the spectral lines experience more broadening. This de-saturates the Be II 313 nm lines, strengthening them in the 3D calculations. In the 1D calculations, this effect can roughly be accounted for by using a larger microturbulence towards the limb (see the discussions in Steffen et al. 2013 and Takeda 2022); here, the 1D calculations assumed a fixed microturbulence of 1.0 km s^{-1}.

It is interesting to consider how the 3D non-LTE versus 1D LTE abundance corrections compare against the combination of the 3D LTE versus 1D LTE abundance corrections and the 1D non-LTE versus 1D LTE abundance corrections. These are shown in Figure 2. Although the 3D non-LTE versus 1D LTE abundance corrections fall in between the two, they do not match up exactly; this discrepancy reflects the coupling of the 3D effects with the non-LTE effects. At the limb, at A(Be) = 1.18, the 3D non-LTE versus 1D LTE abundance correction is −0.03 dex. The 3D LTE versus 1D LTE abundance correction is −0.08 dex and the 1D non-LTE versus 1D LTE abundance correction is 0.09 dex; combining the two gives +0.01 dex, which

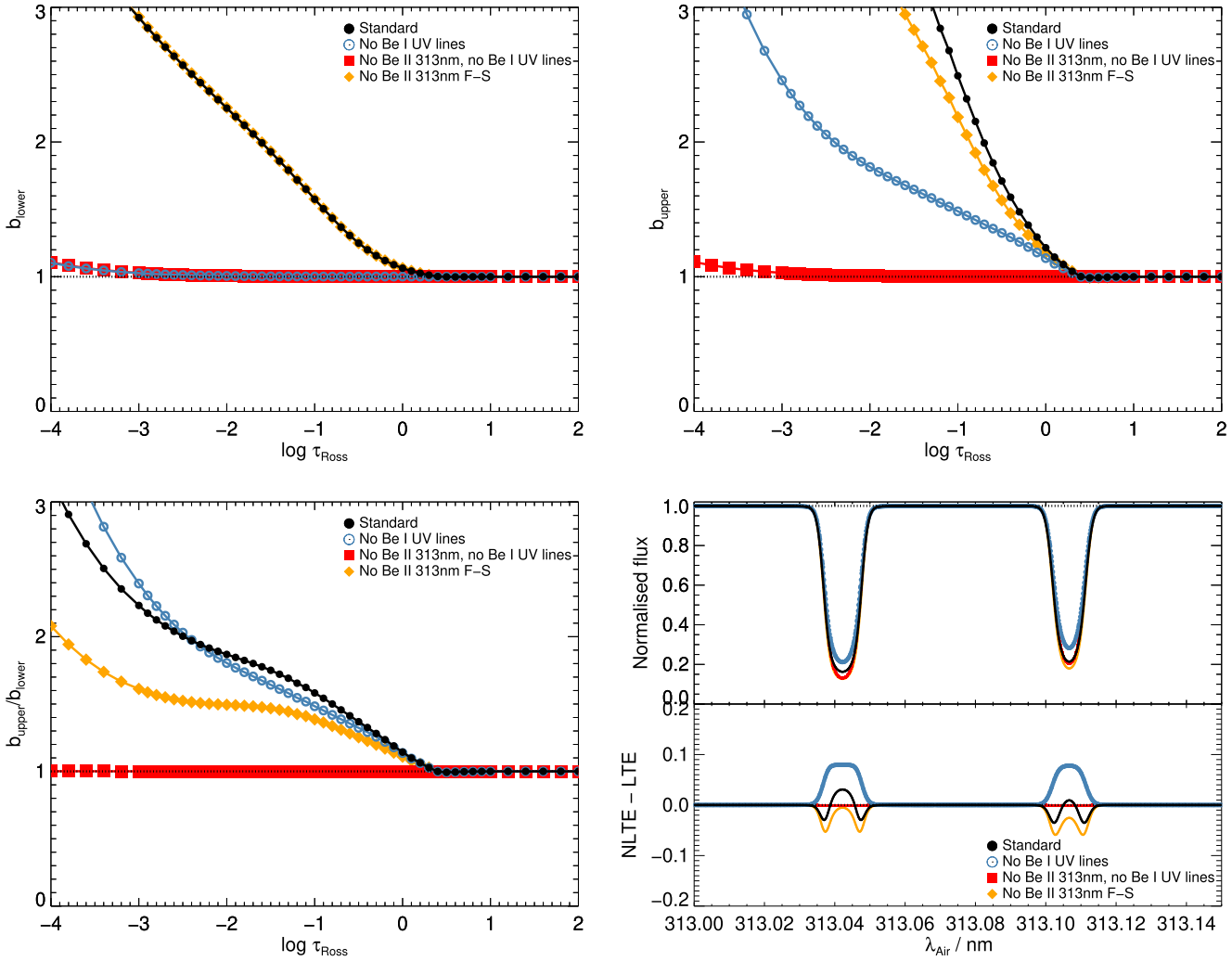

Fig. 4. 1D non-LTE effects on populations and emergent fluxes. Departure coefficients for the lower (upper left panel) and upper (upper right panel) levels of the Be II 313 nm lines as a function of the logarithmic Rosseland mean optical depth, for the standard model (black circles and lines), as well as with different ingredients in the model atom switched off in the statistical equilibrium calculations: the standard model without any Be I UV lines (blue open circles and lines); the same, but also without the Be II 313 nm lines (red squares and lines); and the standard model without fine structure splitting of the Be II 313 nm lines considered in the calculation of J_ν and subsequently when evaluating the radiative rates (No Be II 313 nm F-S; orange diamonds and lines). Also shown are ratios of upper to lower departure coefficients (lower left panel), and the effects on the Be II 313 nm lines as viewed in the emergent disc-integrated flux albeit without rotational broadening or macroturbulence (lower right panel). These calculations are based on the 1D MARCS model atmosphere and A(Be) = 1.18.

is 0.04 dex away from the 3D non-LTE result. This discrepancy becomes larger at other abundances: at very low abundances, A(Be) = 0.38 for example, the discrepancy reaches 0.09 dex.

The coupling between the 3D effects and the non-LTE effects can also be seen on the departure coefficients upon closer inspection of Figure 3. In particular, the $1s^2 2s2p\,{}^1P^o$ level of neutral beryllium (first row, third column) shows an overpopulation around a logarithmic Rosseland mean optical depth of −1 in the 1D calculations; whereas this level is systematically underpopulated in the 3D model at those depths.

3. Analysis of the solar beryllium abundance

The solar beryllium abundance was determined by fitting the 3D non-LTE models described in Section 2 to observed spectra. These fits proceeded in three steps.

In the first step (Section 3.1), the effect of missing continuous opacity on the theoretical disc-integrated flux was calibrated. In the second step (Section 3.2), the wavelength and oscillator strength of the blend at around 313.102 nm was calibrated on disc-centre and limb observations. With these calibrations in hand, in the third step (Section 3.3) the Be II 313.107 nm line was fit to the solar flux data to obtain an inferred value of the solar beryllium abundance and an uncertainty. The spectral line fits were performed by χ^2 minimisation using `MPFIT` (Markwardt 2009).

Each step is based on different observational data presented in the literature. We show the solar irradiance data (converted to solar flux at the stellar surface) in Figure 5, and the continuum-normalised disc-centre and limb intensities as well as disc-integrated flux in Figure 6. All of these data were taken with the McMath-Pierce solar telescope at the Kitt Peak National Observatory, via Chmielewski et al. (1975) and Kurucz (2005). The Fourier Transform Spectrograph has a nominal resolving power of around $R = 3 \times 10^5$.

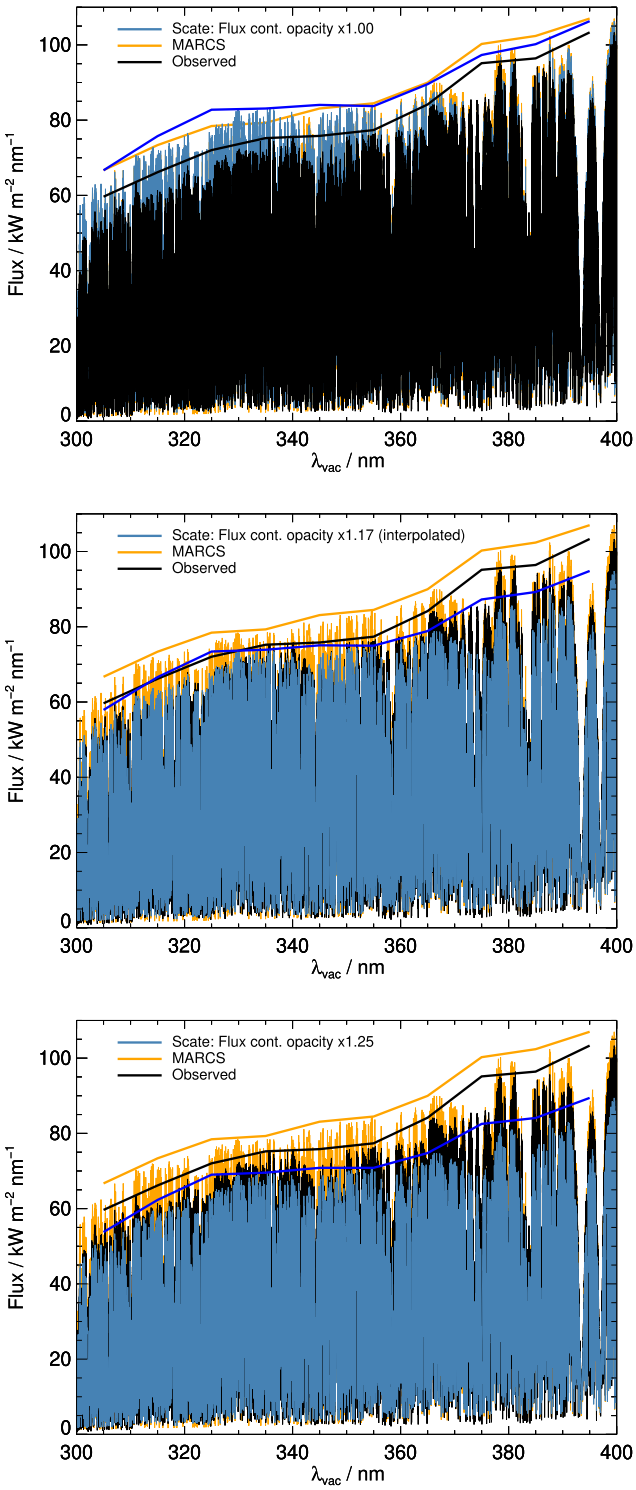

Fig. 5. Disc-integrated flux at the solar surface. Two sets of theoretical data are shown: the `Scate` data are from this work, while the `MARCS` data are from Gustafsson et al. (2008). Also shown are results derived from the solar irradiance atlas of Kurucz (2005). The `Scate` data are shown without any scaling of the continuous opacity (top panel), and with a factor of 1.25 applied (bottom panel), as well as with a factor of 1.17 applied as determined by interpolation (middle panel). The continua are approximately traced by taking maxima within bins of widths of 10 nm.

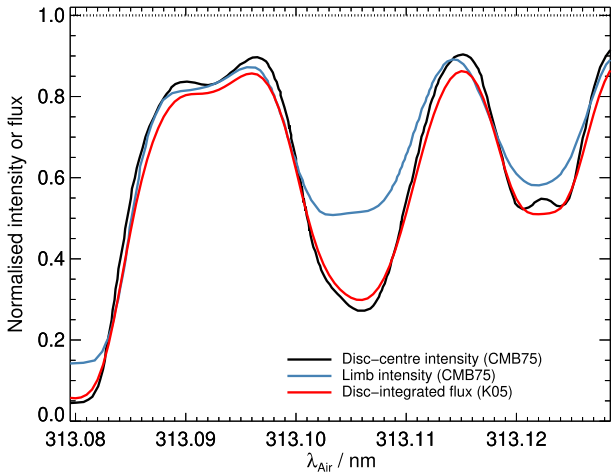

Fig. 6. Continuum-normalised observational data used for spectral line fitting, over-plotted for comparison. Disc-centre and limb intensities from Chmielewski et al. (1975), and disc-integrated flux from Kurucz (2005). All spectra are plotted as a function of wavelength in air and are already corrected for the solar gravitational redshift.

3.1. Step 1: Missing continuous opacity calibration

The solar irradiance atlas presented by Kurucz (2005) was used to calibrate the effect of the missing continuous opacity on the theoretical disc-integrated flux[3]. We illustrate this in Figure 5. It is clear that the continuum flux is slightly too high in the models used in this work, as well as in for instance the fluxes released by Gustafsson et al. (2008) for their solar model. We also illustrate the results after applying a scale factor of 1.25 to the continuous opacity, which is seen to be a slight overcorrection. Interpolating between the two results, the scale factor is roughly 1.17 in the Be II 313.107 nm region. The uncertainty of this scaling factor was estimated to be 0.05 based on different continuum placements, and by itself corresponds to a 0.02 dex uncertainty in A(Be), and neglecting the missing opacity entirely when fitting the disc-integrated flux would reduce the inferred abundance by 0.065 dex.

This method of calibration is inspired by that of Korotin & Kučinskas (2022), but here we make the point of using high-resolution data. Low-resolution data are significantly depressed by spectral lines, as shown in the top panel of Figure 13 of Zhou et al. (2023) for example. This would have made the calibration also dependent on a complete and accurate description of spectral lines: an incomplete line list would lead to an overestimation of the missing continuous opacity.

An alternative, and independent, approach to calibrating the missing continuous opacity is to enforce consistency between oxygen abundances inferred from OH lines in the UV and in the infrared (Balachandran & Bell 1998; Asplund 2004). This approach is prone to uncertainties in the oxygen abundance itself (Carlberg et al. 2018), and to imprecision (and possibly systematic biases) due to difficulties in placing the continuum and in taking blends into account. Moreover, any departures from LTE could affect the UV lines more than the infrared lines (Hinkle & Lambert 1975; see also the discussion in Section 2.5.2 of Lind & Amarsi 2024), the effect of which would conflate with that of the missing continuous opacity. Nevertheless, it is reassuring that the enhancement of 1.17 derived here closely agrees with the value of 1.2 obtained in Section 3 of Carlberg et al. (2018) using the OH method, although this could be a coincidence due to the different tools and atomic data being used.

[3] http://kurucz.harvard.edu/sun/irradiance2005/irradthu.dat

The enhancement to the continuous opacity is expected to have a centre-to-limb variation itself, and the value of 1.17 derived here only applies to the disc-integrated flux. Looking towards the limb, the contribution of metal opacity becomes larger and the hydrogen opacity becomes smaller. If the metal photoionisation cross-sections are underestimated then the overall continuous opacity scale factor must increase towards the limb. An alternative approach to that adopted here is to correct the metal photoionisation cross-sections directly (e.g. Korotin & Kučinskas 2022); in this case the scale factor would not change drastically going from disc-centre to the limb.

3.2. Step 2: Line list and blend calibration

Following Korotin & Kučinskas (2022), the VALD database was used to generate a theoretical line list to describe the Be II 313.107 nm region. This line list includes 74 known blends plus the Be II line itself; the blue-most line is the strong Ti II 313.080 nm, and the red-most line is the Tm II 313.126 nm. Repeating the entire analysis without any lines except for the Be II 313.107 nm and the calibrated hypothetical line discussed below changed the overall result by just +0.037 dex. Half of this value was folded into the uncertainty on the overall result (Section 3.3).

Apart from the hypothetical line discussed below, only one empirical and two theoretical modifications were made to this initial line list. The empirical modification was for the position of the Cr I line that blends the red wing of the Be II 313.107 nm. It was shifted from its nominal laboratory wavelength of 313.1216 nm to the value given in Chmielewski et al. (1975), namely 313.1207 nm. The theoretical modifications concern the parameters for broadening due to elastic collisions with neutral hydrogen (usually referred to as van der Waals broadening) for the Ti II 313.080 nm and Cr I 313.121 nm lines that perturb the wings of the Be II 313.107 nm feature. In this work, these were calculated using ABO theory. The Ti II line broadening was calculated with the theory extended to singly ionised species as in Barklem & O'Mara (1998), assuming the Unsöld approximation value for the parameter $E_p = -4/9$ atomic units, which should be expected to be a reasonable approximation for most lines (see Figure 2 of Barklem & Aspelund-Johansson 2005). The Cr I line broadening was calculated with the theory as presented in Anstee & O'Mara (1995). The recommended numbers are $\{\sigma, \alpha\} = \{217\,a_0^2, 0.213\}$ and $\{415\,a_0^2, 0.262\}$ respectively, where σ is the broadening cross-section at reference velocity $v = 10^4\,\mathrm{m\,s^{-1}}$, and α is the dimensionless exponent of the velocity scale factor $v^{-\alpha}$. These parameters were found to improve the quality of the fits compared to the LFU theory with no enhancement factor.

The most influential adjustment to the line list was the introduction of a hypothetical line to explain the observed width and asymmetry of the Be II 313.107 nm feature. By analysing the feature in dwarfs and giants, Carlberg et al. (2018) argued that this blend could be caused by a line of an ionised species with a low excitation energy for the lower level of the transition. Chmielewski et al. (1975) arrived at a similar conclusion on analysing the solar centre-to-limb variation. If true, this is fortuitous in the sense that generally weak, low-excitation lines of majority ionised species, typically show small departures from LTE in solar-metallicity dwarfs (e.g. for iron see Amarsi et al. 2022; for titanium see Mallinson et al. 2022, 2024). The authors adopted Ti II with $E_{\mathrm{low}} = 0.01$ eV; and this was adopted in this work. A first guess of the laboratory wavelength was taken from Chmielewski et al. (1975), namely 313.1019 nm.

The disc-centre ($\mu = 1.0$) and limb ($\mu = 0.2$) data presented in Chmielewski et al. (1975) were used to calibrate the wavelength and oscillator strength of the hypothetical Ti II line. These observational data were extracted via a digital conversion from their Figures 5 and 6 respectively. Their continuum placement was adopted without modification, but the wavelengths were shifted to the blue by a velocity of $633\,\mathrm{m\,s^{-1}}$ to correct for the solar gravitational redshift. As discussed in Chmielewski et al. (1975), the asymmetry in the Be II 313.107 nm feature can be clearly seen in the line intensities, which are not broadened by solar rotation. This facilitates a more robust calibration of the blend, especially when combined with 3D non-LTE models, which incorporate other line asymmetries due to solar surface convection and for which microturbulence and macroturbulence do not need to be calibrated. As we mentioned at the start of the present Section, the nominal resolving power of the spectrograph is $R = 3 \times 10^5$. In the analysis the theoretical spectra were broadened using a sinc^2 kernel of full width at half maximum λ/R, and this led to an improved fit for the line wings.

The calibration proceeded as follows. The Chmielewski et al. (1975) observations at disc-centre ($\mu = 1.0$) and at the limb ($\mu = 0.2$) were fit simultaneously. The fit initially had five free parameters. Three of them, namely the beryllium abundance, and the oscillator strength and the wavelength of the hypothetical Ti II line, were constrained to be the same at both pointings. The other two free parameters were the missing continuous opacity factors, at disc-centre and at the limb. These were allowed to vary between the two pointings because the missing continuous opacity has a centre-to-limb variation itself: there is an increasing contribution of metal opacity towards the limb as we discussed in Section 3.1. We note that the initial best-fitting beryllium abundance from this analysis of the disc-centre and limb alone was $A(\mathrm{Be}) = 1.16$. Afterwards, the calibration was repeated but with the beryllium abundance constrained to the best-fitting value following the analysis of the disc-integrated flux (Section 3.3); this was iterated until convergence was achieved. Folding in the disc-integrated flux, for which we directly calibrated the missing opacity (Section 3.1), raises the inferred beryllium abundance to our final value of $A(\mathrm{Be}) = 1.21$ as we discuss in Section 3.3.

We show the fits in Figure 7, along with the fitting mask. Apart from the hypothetical blend, the blue wing of the Be II 313.107 nm line is perturbed by the strong Ti II 313.080 nm line together with a weaker OH line at 313.093 nm. At disc-centre, these features are reproduced well by the models. Consequently, expanding the fitting region by 0.005 nm to include the far blue wing of the feature had a negligible change on the calibrated oscillator strength of the blend. The agreement for the red wing is less good, but remains satisfactory and is an improvement over what was found by Chmielewski et al. (1975). There is significant overlap with the weak Zr I 313.111 nm line, and the wing is more strongly perturbed by the combination of the Cr I 313.121 nm, Fe I 313.124 nm, and Tm II 313.126 nm lines The first of these, the Zr I 313.111 nm line, was discussed by Carlberg et al. (2018) who suggested to reduce its oscillator strength. Doing so would only slightly decrease the beryllium abundance inferred in this study. At the far limb, the blue wing is reproduced much better than the red wing. This could reflect the growing importance of non-LTE effects towards the limb, and how the Ti II and OH lines on the blue wing form relatively close to LTE. The minority species Cr I and Fe I on the red wing are expected to suffer from overionisation, and these lines may therefore appear weaker if modelled in 3D non-LTE.

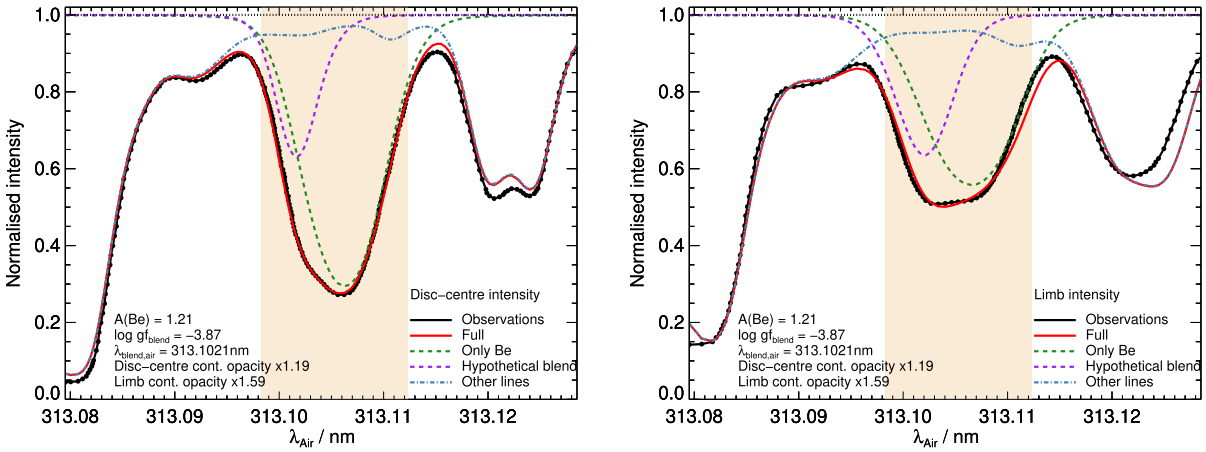

Fig. 7. Fits to the disc-centre (left panel) and limb (right panel) intensities resulting from the calibration of the blend described in Section 3.2. The shaded area shows the wavelength range considered in the fit.

The main limitation of this calibration arises from the treatment of the missing continuous opacities at disc-centre and at the limb. These were allowed to vary freely and separately, and this could compensate for residual deficiencies in the 3D non-LTE models of the centre-to-limb variation. While 3D non-LTE models consistently outperform 3D LTE, 1D non-LTE, and especially 1D LTE models (e.g. Lind et al. 2017; Canocchi et al. 2024), it is possible that improved physics are needed to obtain more accurate results, such as magnetic fields (Ludwig et al. 2023; Kostogryz et al. 2024). Forcing the beryllium abundance and the blend parameters to be the same at disc-centre and the limb helps mitigate the possible effects of this and helps to get a more reliable calibration for the blend. As a limiting test, the analysis was repeated forcing the continuous opacity scale factors at disc-centre and limb to be that calibrated for the disc-integrated flux, 1.17 (Section 3.1). The fits in that case were poor at the limb; nevertheless, the overall solar beryllium abundance changed by only +0.049 dex. Half of this value was folded into the uncertainty on the overall result (Section 3.3).

We show the final line list in Table 1. The provided line list includes the empirical modifications and calibrations discussed above.

3.3. Step 3: The solar beryllium abundance and its uncertainty

With the calibration for the missing continuous opacity in the disc-integrated flux (a factor of 1.17 applied to the continuous opacity in the spectrum synthesis with `Scate`; see Section 3.1) and parameters for the blending line calibrated on the centre-to-limb variation (tuned wavelength and oscillator strength; see Section 3.2), the solar beryllium abundance was derived by fitting the high resolution solar flux atlas from Kurucz (2005), which is a re-reduction of the atlas of Kurucz et al. (1984)[4]. The continuum was placed by comparison with the normalised centre and limb spectra from Chmielewski et al. (1975). Rotational broadening was taken into account in the theoretical spectra following Section 2 of Dravins & Nordlund (1990), adopting $v \sin \iota = 2.0\,\mathrm{km\,s^{-1}}$ (dos Santos et al. 2016). Like with the intensities (Section 3.2), these rotationally broadened disc-integrated fluxes were then broadened further using a sinc^2 kernel of full width at half maximum λ/R, with $R = 3 \times 10^5$.

[4] http://kurucz.harvard.edu/sun/fluxatlas2005/solarfluxintwl.asc

We show the fit in Figure 8. The best-fitting value for the solar beryllium abundance is 1.21 ± 0.05 dex. This value is significantly lower than the value of Asplund et al. (2021), 1.38 ± 0.09, in large part because the original analysis in Asplund (2004) neglected the impact of the hypothetical blend as we discussed in Section 1. It is also lower than values obtained by other recent 1D LTE and 1D non-LTE studies (Carlberg et al. 2018; Korotin & Kučinskas 2022), of around 1.30 to 1.35 dex, which we attribute primarily to differences in the calibration strategy: our value is closer to the value of 1.15 dex found by Chmielewski et al. (1975) who also calibrated the blend on high-resolution observations of the disc-centre and limb intensities, albeit in 1D non-LTE and with a small nine-level model atom.

The uncertainty of 0.05 dex was estimated by first running 1000 further fits perturbing different ingredients by drawing from independent Gaussian distributions of different standard deviations σ and taking the standard deviation of the 1000 resulting beryllium abundances. The ingredients that varied were the scale factor for the continuous opacity ($\sigma = 0.05$; as we discussed in Section 3.1), as well as a scale factor for the continuum placement ($\sigma = 0.03$). The resulting uncertainty was 0.036 dex. Secondly, the uncertainty caused by other blending lines was estimated as half the difference with the abundance obtained by repeating the entire analysis without any blends apart from the calibrated one (as we discussed in Section 3.2); this gave 0.018 dex. Lastly, the effect of the uncertainty in the blend calibration was estimated as half the difference with the result obtained when the continuous opacity scale factors at disc-centre and limb were fixed at 1.17 (as we discussed in Section 3.2); this gave 0.025 dex. The final uncertainty estimate was obtained by adding these three numbers in quadrature.

4. The depletion of beryllium in comparison with solar model predictions

The extra depletion of beryllium in the solar surface (on top of any effects of atomic diffusion) is estimated to be −0.11 ± 0.06 dex, or 22 ± 11%, when taking $A(\mathrm{Be}) = 1.21 \pm 0.05$ that we found in Section 3, and $A(\mathrm{Be})_{\mathrm{init}} = 1.32 \pm 0.04$ as we discussed in Section 1. In this section we compare these results to predictions from a standard solar model (SSM) as well as a solar model that includes the effects of angular momentum transport ($\mathrm{D_R}$), both computed using the Liège stellar evolution code (CLES; Scuflaire et al. 2008).

Table 1. Line list adopted for the synthesis of the Be II 313.107 nm region.

Species	$\lambda_{\rm Air}$/nm	$E_{\rm low}$/eV	log gf	A(X)	Species	$\lambda_{\rm Air}$/nm	$E_{\rm low}$/eV	log gf	A(X)
[a]Ti II	313.079869	0.0117	−1.190	4.97	Mn I	313.103629	3.7723	−1.667	5.42
Ce II	313.080457	0.8085	−1.830	1.58	CN	313.104785	0.9476	−6.251	8.47/7.89
Ar I	313.080815	11.5484	−2.910	6.38	Ar I	313.105415	11.5484	−3.780	6.38
CN	313.081074	0.9612	−2.987	8.47/7.89	CN	313.105501	1.2900	−6.588	8.47/7.89
Gd II	313.081315	1.1566	−0.083	1.08	Fe II	313.105884	9.7002	−3.717	7.46
OH	313.081359	1.9392	−3.782	8.70/12.00	Mn II	313.105933	6.6711	−2.692	5.42
Co II	313.081830	9.2397	−6.551	4.94	V II	313.106325	4.2438	−4.386	3.90
CN	313.081830	0.3326	−4.245	8.47/7.89	[c]Be II	313.106516	0.0000	−0.479	1.21
Cu I	313.083154	6.1920	−6.851	4.18	CN	313.106737	1.2900	−6.195	8.47/7.89
CN	313.083154	0.9612	−6.261	8.47/7.89	Th II	313.107016	0.0000	−1.559	0.03
CN	313.083889	0.3326	−4.272	8.47/7.89	Fe II	313.109032	11.2065	−5.030	7.46
V I	313.084164	1.9553	−3.762	3.90	[d]Cr II	313.110022	8.5981	−2.636	5.62
Cr II	313.084350	10.7484	−6.564	5.62	[e]Fe II	313.110425	9.6878	−1.036	7.46
Ce II	313.085183	0.0000	−3.010	1.58	Fe I	313.111013	3.0469	−5.610	7.46
Cu I	313.086997	6.1227	−2.728	4.18	Zr I	313.111016	0.5203	−0.400	2.59
Fe II	313.087056	8.9593	−5.404	7.46	CO	313.111229	5.2067	−6.164	8.47/7.89
Ce II	313.087086	1.0897	−2.250	1.58	Os I	313.111616	1.8409	+0.050	1.35
Ce II	313.087586	1.1069	−0.320	1.58	CN	313.112102	0.7697	−3.352	8.47/7.89
Cr II	313.088723	9.5803	−2.745	5.62	V II	313.112307	6.5807	−5.242	3.90
Cu I	313.090076	6.1227	−3.697	4.18	Ti I	313.114298	0.8360	−6.733	4.97
Fe II	313.090478	7.4867	−2.429	7.46	CN	313.114475	0.7698	−6.763	8.47/7.89
CN	313.092136	0.2947	−4.364	8.47/7.89	CN	313.114544	1.0137	−6.561	8.47/7.89
Ce II	313.092185	0.4954	−0.760	1.58	CN	313.115515	0.5037	−5.142	8.47/7.89
OH	313.093341	0.6832	−3.359	8.70/12.00	CN	313.115613	0.5037	−4.841	8.47/7.89
CN	313.093518	0.2947	−4.397	8.47/7.89	Mo I	313.119416	2.4992	−1.356	1.88
CN	313.095195	0.0013	−5.882	8.47/7.89	CN	313.119634	0.3414	−4.219	8.47/7.89
CN	313.095744	0.0013	−6.039	8.47/7.89	Cr I	313.119918	3.0106	−6.270	5.62
CN	313.095950	1.2986	−6.176	8.47/7.89	Ni II	313.120545	12.7385	−3.114	6.20
Cr II	313.096950	6.8027	−4.643	5.62	[f]Cr I	313.120692	3.1128	−0.401	5.62
CN	313.097264	0.0127	−5.531	8.47/7.89	CN	313.120947	2.3116	−5.598	8.47/7.89
CN	313.097411	0.0127	−5.594	8.47/7.89	CN	313.121781	0.3414	−4.245	8.47/7.89
OH	313.099275	1.5694	−4.030	8.70/12.00	CN	313.121860	0.9345	−3.005	8.47/7.89
N II	313.099516	20.4091	−3.140	7.83	CN	313.122409	2.3116	−2.454	8.47/7.89
CN	313.099608	0.9476	−2.987	8.47/7.89	CN	313.123665	1.2742	−6.964	8.47/7.89
Mn II	313.101520	6.1113	−1.230	5.42	Fe I	313.124311	2.1759	−3.792	7.46
[b]Ti II	313.102096	0.0100	−3.875	4.97	CN	313.125077	0.9345	−3.023	8.47/7.89
CN	313.102461	0.9978	−6.746	8.47/7.89	CN	313.125145	2.3116	−2.475	8.47/7.89
CN	313.102775	0.9476	−3.005	8.47/7.89	Tm II	313.125515	0.0000	+0.240	0.11

Notes. Lines from the VALD database, with modifications noted below. Adopted elemental abundances from Asplund et al. (2021) for atomic and ionic species, and Amarsi et al. (2021) for the different elements in molecular species of C, N, and O. [a]ABO parameters calculated in this work $\{\sigma, \alpha\} = \{217\,{\rm a}_0^2, 0.213\}$. [b]Hypothetical blend with fitted wavelength and oscillator strength. [c]Beryllium line with fitted abundance, and VALD ABO parameters $\{\sigma, \alpha\} = \{123\,{\rm a}_0^2, 0.212\}$. [d]VALD ABO parameters $\{\sigma, \alpha\} = \{519\,{\rm a}_0^2, 0.213\}$. [e]VALD ABO parameters $\{\sigma, \alpha\} = \{407\,{\rm a}_0^2, 0.284\}$. [f]Wavelength from Chmielewski et al. (1975), and ABO parameters calculated in this work $\{\sigma, \alpha\} = \{415\,{\rm a}_0^2, 0.262\}$.

The D_R model includes the combined effects of hydrodynamical and magnetic instabilities following an asymptotic formalism introduced in Buldgen et al. (2024). This analytical expression allows to capture the full effects of the combined meridional circulation, shear-induced turbulence and magnetic Tayler instability (Spruit 2002) on the depletion of light elements. In Eggenberger et al. (2022), the combination of these physical mechanisms was used to explain simultaneously the solar rotation profile, the observed photospheric lithium depletion and an increased helium mass fraction in the solar convective zone. Compared to the model of Eggenberger et al. (2022) based on the Geneva stellar evolution code (GENEC; Eggenberger et al. 2008), the CLES model used here predicts a larger amount of beryllium depletion. This is caused by a combination of factors, including differences in the nuclear reaction network between the two codes, as well as different reference solar abundances – rather than Asplund et al. (2009), the CLES model used here is based on the compilation of Asplund et al. (2021), which is overall more metal-rich and also has a 0.09 dex lower lithium abundance (via Wang et al. 2021).

We illustrate the predicted evolution of the surface abundance of beryllium in Figure 9. The initial chemical compositions of the two models do not match exactly, as they are free parameters in the models and thus are sensitive to the different input physics. As such, the relevant quantity to inspect in these plots is the relative difference between the initial and final beryllium abundances (i.e. the beryllium depletion itself). It turns out that neither the SSM nor the D_R model can reproduce the beryl-

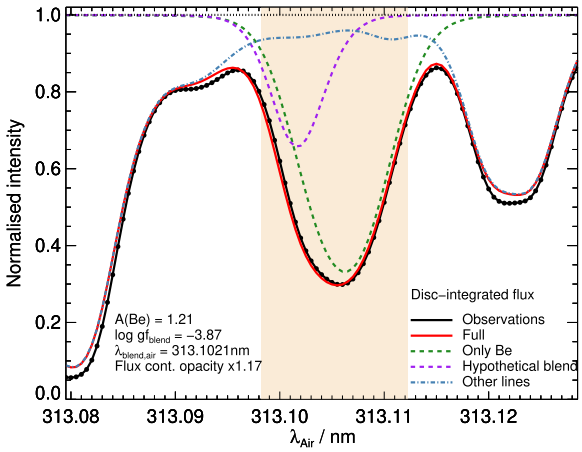

Fig. 8. Fit to the disc-integrated flux described in Section 3.3, based on the continuous opacity calibration in Section 3.1 and blend calibration in Section 3.2. The shaded area shows the wavelength range considered in the fit.

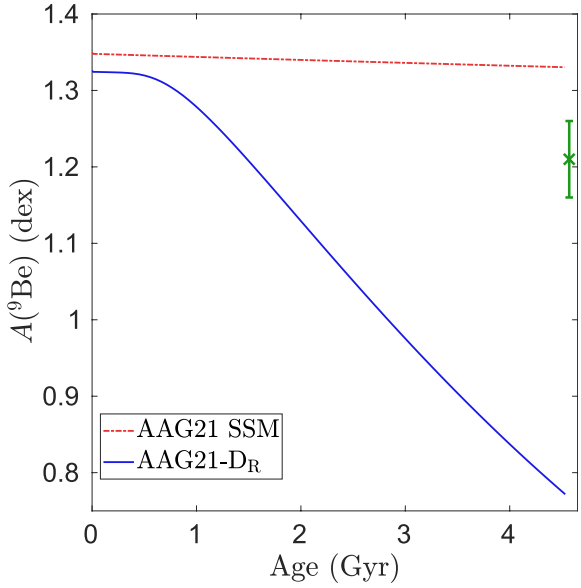

Fig. 9. Predicted evolution of the surface beryllium abundance with different theoretical models. Red shows a standard solar model (SSM); blue shows a model that includes the effects of angular momentum transport (D_R). The point at 4.6 Gyr shows the current value of the surface beryllium abundance that was determined in Section 3.3.

lium depletion reported in this work: the former predicts negligible depletion, while the latter predicts a depletion of more than 0.5 dex (roughly a factor of three).

One possible explanation is that the initial solar beryllium abundance is in error. The adopted value of $A(\mathrm{Be})_{\mathrm{init}} = 1.32 \pm 0.04$ via Lodders (2021) is based on the Orgueil meteorite. The analysis of the Ivuna meteorite by King et al. (2020) gives a larger beryllium abundance: $A(\mathrm{Be})_{\mathrm{init}} = 1.38 \pm 0.04$, using silicon, magnesium, and iron to convert the meteoritic abundances onto the solar scale (see Section 1). As discussed therein, Ivuna is possibly less affected by terrestrial modification. However, The two meteorites typically agree well, with a mean difference in X/Si ratios of -0.02 ± 0.03 dex for 52 elements in common, and the discrepancy could be due to the heterogeneous nature of CI chondrites and the small sample size of the Ivuna meteorite. In any case, using the result from the Ivuna meteorite the beryllium depletion in the Sun would be 0.17 ± 0.04, which is still far less than that predicted by the D_R model. We also note that the effects of atomic diffusion are neglected in the conversion from the meteoritic abundance scale to the solar abundance scale in Section 1. This may amount to a 0.03 dex to 0.06 dex larger value of $A(\mathrm{Be})_{\mathrm{init}}$ (see Section 5 of Asplund et al. 2021). Nevertheless, the corresponding depletion values would still be far too low to be explained by the D_R model.

The failure of the D_R model is not too surprising as the so-called Tayler-Spruit instability has proven unable to reproduce asteroseismic constraints on the internal rotation of young solar-like subgiants (Deheuvels et al. 2020). Further investigations will be required to determine whether a combination of other processes such as overshooting or opacity increases at the base of the solar convective zone, as investigated in Ayukov & Baturin (2017), Buldgen et al. (2019), and Kunitomo et al. (2022), will be able to reconcile these new solar models with observations.

Detailed comparisons between various evolution codes (e.g. Deal, in prep.) will shed new light on the predicted light element depletions in the context of the solar modelling problem. Nevertheless, the observed depletion of beryllium in the Sun advocates for some form of turbulent mixing at the base of the solar convective zone acting during the main-sequence, in disagreement with the prescriptions used in Standard Solar Models that only consider microscopic diffusion. After having calibrated the transport coefficients on the solar depletion, it might also be interesting to apply them to solar twins, such as the 16 Cyg binary system (Farnir et al. 2020; Buldgen et al. 2022) for which Deal et al. (2015) used the light element depletion as a tracer of planetary accretion.

5. Conclusions

We have presented 3D non-LTE calculations for beryllium in the solar atmosphere, and have used the models to determine the present-day abundance of beryllium in the solar surface. The analysis presented here combines and builds upon ideas presented separately in the literature: it uses the observed solar irradiance to calibrate the missing opacity (Korotin & Kučinskas 2022), the centre-to-limb variation to calibrate the blend (Chmielewski et al. 1975), which in turn is assumed to be a low-excitation line of an ionised majority species based on the analyses of Chmielewski et al. (1975) and Carlberg et al. (2018).

We found $A(\mathrm{Be}) = 1.21 \pm 0.05$ for the present-day surface abundance. The initial abundance was taken to be $A(\mathrm{Be})_{\mathrm{init}} = 1.32 \pm 0.04$ based on the CI chondrite Orgueil and converted to the solar scale using silicon, magnesium, and iron and neglecting the possible impact of atomic diffusion; although we note that a recent analysis of the CI chondrite Ivuna could indicate an even larger initial abundance. With this initial value we found that beryllium has been depleted by an extra 0.11 ± 0.06 dex, or $22 \pm 11\%$, on top of any effects of atomic diffusion. This is in tension with Standard Solar Models, which predict negligible depletion, as well as contemporary solar models with calibrated extra mixing (e.g. Eggenberger et al. 2022), which predict excessive depletion; the non-Standard model used here predicts a depletion in excess of 0.5 dex, for example.

To even better pin down the solar beryllium abundance in the near future, tighter constraints on the line list would be welcome. This could be tackled empirically, for example by studying other stars of different stellar parameters like in Carlberg et al. (2018), but using 3D non-LTE models to avoid the microturbulence or macroturbulence fudge parameters that could hamper calibrations. Furthermore, improved 3D non-LTE modelling of the centre-to-limb variation, for example using models including magnetic fields (Ludwig et al. 2023; Kostogryz et al. 2024),

would help ensure that the calibration presented here is indeed reliable. On longer timescales, a better first-principles description of the continuous opacity in the UV as well as a concrete identification of the 313.102 nm blend are sorely needed. In particular, theoretical atomic structure calculations could perhaps shed light on the identity of the blending feature, for instance to confirm or rule out the Mn I 313.104 nm line as a contender. In the meantime, we make the 3D LTE and 3D non-LTE spectra used in this work publicly available (online Table 2) so that others may use them to explore different calibration strategies.

Data availability

Table 2 is available at the CDS via anonymous ftp to cdsarc.cds.unistra.fr (130.79.128.5) or via https://cdsarc.cds.unistra.fr/viz-bin/cat/J/A+A/690/A128

Acknowledgements. The authors wish to thank S. Korotin for providing a constructive referee report. AMA acknowledges support from the Swedish Research Council (VR 2020-03940) and from the Crafoord Foundation via the Royal Swedish Academy of Sciences (CR 2024-0015). GB is funded by an Fonds National de La Recherche Scientifique (FNRS) postdoctoral fellowship. YZ gratefully acknowledges support from the Elaine P. Snowden Fellowship. PSB acknowledges support from the Swedish Research Council (VR 2020-03404). This research was supported by computational resources provided by the Australian Government through the National Computational Infrastructure (NCI) under the National Computational Merit Allocation Scheme and the ANU Merit Allocation Scheme (project y89). Some of the computations were also enabled by resources provided by the National Academic Infrastructure for Supercomputing in Sweden (NAISS), partially funded by the Swedish Research Council through grant agreement no. 2022-06725, at the PDC Center for High Performance Computing, KTH Royal Institute of Technology (project number PDC-BUS-2022-4).

References

Allen, C. W. 1973, Astrophysical Quantities (London: University of London, Athlone Press)
Amarsi, A. M., Lind, K., Asplund, M., Barklem, P. S., & Collet, R. 2016, MNRAS, 463, 1518
Amarsi, A. M., Barklem, P. S., Asplund, M., Collet, R., & Zatsarinny, O. 2018a, A&A, 616, A89
Amarsi, A. M., Nordlander, T., Barklem, P. S., et al. 2018b, A&A, 615, A139
Amarsi, A. M., Barklem, P. S., Collet, R., Grevesse, N., & Asplund, M. 2019, A&A, 624, A111
Amarsi, A. M., Grevesse, N., Grumer, J., et al. 2020, A&A, 636, A120
Amarsi, A. M., Grevesse, N., Asplund, M., & Collet, R. 2021, A&A, 656, A113
Amarsi, A. M., Liljegren, S., & Nissen, P. E. 2022, A&A, 668, A68
Anders, E., & Grevesse, N. 1989, Geochim. Cosmochim. Acta, 53, 197
Anstee, S. D., & O'Mara, B. J. 1995, MNRAS, 276, 859
Ashwell, J. F., Jeffries, R. D., & Smalley, B. 2005, Mem. Soc. Astron. It. Suppl., 8, 206
Asplund, M. 2004, A&A, 417, 769
Asplund, M., Grevesse, N., Sauval, A. J., & Scott, P. 2009, ARA&A, 47, 481
Asplund, M., Amarsi, A. M., & Grevesse, N. 2021, A&A, 653, A141
Ayukov, S. V., & Baturin, V. A. 2017, Astron. Rep., 61, 901
Balachandran, S. C., & Bell, R. A. 1998, Nature, 392, 791
Barklem, P. S. 2016a, A&ARv, 24, 9
Barklem, P. S. 2016b, Phys. Rev. A, 93, 042705
Barklem, P. S., & Aspelund-Johansson, J. 2005, A&A, 435, 373
Barklem, P. S., & O'Mara, B. J. 1997, MNRAS, 290, 102
Barklem, P. S., & O'Mara, B. J. 1998, MNRAS, 300, 863
Barklem, P. S., & O'Mara, B. J. 2000, MNRAS, 311, 535
Barklem, P. S., O'Mara, B. J., & Ross, J. E. 1998, MNRAS, 296, 1057
Belyaev, A. K. 2013, Phys. Rev. A, 88, 052704
Boesgaard, A. M. 2023, ApJ, 943, 40
Bray, I., & Stelbovics, A. T. 1992, Phys. Rev. A., 46, 6995
Buldgen, G., Salmon, S. J. A. J., Noels, A., et al. 2019, A&A, 621, A33
Buldgen, G., Farnir, M., Eggenberger, P., et al. 2022, A&A, 661, A143
Buldgen, G., Eggenberger, P., Noels, A., et al. 2023, A&A, 669, L9
Buldgen, G., Noels, A., Scuflaire, R., et al. 2024, A&A, 686, A108
Canocchi, G., Lind, K., Lagae, C., et al. 2024, A&A, 683, A242
Carlberg, J. K., Cunha, K., Smith, V. V., & do Nascimento, J., 2018, ApJ, 865, 8
Castelli, F., & Kurucz, R. L. 2003, in Modelling of Stellar Atmospheres, eds. N. Piskunov, W. W. Weiss, & D. F. Gray, 210, A20
Chmielewski, Y., Brault, J. W., & Mueller, E. A. 1975, A&A, 42, 37
Christensen-Dalsgaard, J. 2021, Liv. Rev. Sol. Phys., 18, 2
Collet, R., Magic, Z., & Asplund, M. 2011, J. Phys. Conf. Ser., 328, 012003
Cunto, W., Mendoza, C., Ochsenbein, F., & Zeippen, C. J. 1993, A&A, 275, L5
Deal, M., Richard, O., & Vauclair, S. 2015, A&A, 584, A105
Deheuvels, S., Ballot, J., Eggenberger, P., et al. 2020, A&A, 641, A117
Delgado Mena, E., Israelian, G., González Hernández, J. I., Santos, N. C., & Rebolo, R. 2012, ApJ, 746, 47
Dipti, Das, T., Bartschat, K., et al. 2019, At. Data Nucl. Data Tab., 127, 1
Dipti, Bray, I., Fursa, D. V., et al. 2024, At. Data Nucl. Data Tab., 156, 101634
dos Santos, L. A., Meléndez, J., do Nascimento, J.-D.et al. 2016, A&A, 592, A156
Dravins, D., & Nordlund, A. 1990, A&A, 228, 203
Eggenberger, P., Meynet, G., Maeder, A., et al. 2008, Ap&SS, 316, 43
Eggenberger, P., Buldgen, G., Salmon, S. J. A. J., et al. 2022, Nat. Astron., 6, 788
Farnir, M., Dupret, M. A., Buldgen, G., et al. 2020, A&A, 644, A37
Garcia Lopez, R. J., Severino, G., & Gomez, M. T. 1995, A&A, 297, 787
Gonzalez, G. 1997, MNRAS, 285, 403
Gonzalez, G., Carlson, M. K., & Tobin, R. W. 2010, MNRAS, 407, 314
Gustafsson, B., Edvardsson, B., Eriksson, K., et al. 2008, A&A, 486, 951
Hayek, W., Asplund, M., Collet, R., & Nordlund, Å. 2011, A&A, 529, A158
Heiter, U., Barklem, P., Fossati, L., et al. 2008, J. Phys. Conf. Ser., 130, 012011
Hinkle, K. H., & Lambert, D. L. 1975, MNRAS, 170, 447
Holweger, H., & Müller, E. A. 1974, Sol. Phys., 39, 19
Kaulakys, B. P. 1985, J. Phys. B, 18, L167
Kaulakys, B. P. 1986, JETP, 91, 391
Kaulakys, B. P. 1991, J. Phys. B, 24, L127
King, A. J., Phillips, K. J. H., Strekopytov, S., Vita-Finzi, C., & Russell, S. S. 2020, Geochim. Cosmochim. Acta, 268, 73
Korotin, S., & Kučinskas, A. 2022, A&A, 657, L11
Kostogryz, N. M., Shapiro, A. I., Witzke, V., et al. 2024, Nat. Astron., 8, 929
Kunitomo, M., Guillot, T., & Buldgen, G. 2022, A&A, 667, L2
Kurucz, R. L. 2005, Mem. Soc. Astron. It. Suppl., 8, 189
Kurucz, R. L., Furenlid, I., Brault, J., & Testerman, L. 1984, Solar Flux Atlas from 296 to 1300 nm (New Mexico: NSO)
Lambert, D. L. 1993, Phys. Scr. Vol. T, 47, 186
Lamia, L., Spitaleri, C., Tognelli, E., et al. 2015, ApJ, 811, 99
Leenaarts, J., & Carlsson, M. 2009, ASP Conf. Ser., 415, 87
Lind, K., & Amarsi, A. M. 2024, ARA&A, in press [arXiv:2401.00697]
Lind, K., Amarsi, A. M., Asplund, M., et al. 2017, MNRAS, 468, 4311
Lodders, K. 2021, Space Sci. Rev., 217, 44
Lodders, K., Palme, H., & Gail, H. P. 2009, Landolt-Börnstein, 4B, 712
Ludwig, H. G., Steffen, M., & Freytag, B. 2023, A&A, 679, A65
Magic, Z., Collet, R., Asplund, M., et al. 2013, A&A, 557, A26
Mallinson, J. W. E., Lind, K., Amarsi, A. M., et al. 2022, A&A, 668, A103
Mallinson, J. W. E., Lind, K., Amarsi, A. M., & Youakim, K. 2024, A&A, 687, A5
Markwardt, C. B. 2009, ASP Conf. Ser., 411, 251
Ogneva, D. 2023, Bachelor's Thesis, Uppsala University, Sweden
Primas, F., Duncan, D. K., Pinsonneault, M. H., Deliyannis, C. P., & Thorburn, J. A. 1997, ApJ, 480, 784
Ralchenko, Y., & Kramida, A. 2020, Atoms, 8, 56
Rodríguez Díaz, L. F., Lagae, C., Amarsi, A. M., et al. 2024, A&A, 688, A212
Schmidt-May, A. F., Barklem, P. S., Grumer, J., et al. 2024, Phys. Rev. A, 109, 052820
Scuflaire, R., Théado, S., Montalbán, J., et al. 2008, Ap&SS, 316, 83
Smiljanic, R., da Silva, A. R., & Giribaldi, R. E. 2023, Exp. Astron., 55, 95
Spruit, H. C. 2002, A&A, 381, 923
Steffen, M., Caffau, E., & Ludwig, H.-G. 2013, Mem. Soc. Astron. It. Suppl., 24, 37
Steffen, M., Prakapavičius, D., Caffau, E., et al. 2015, A&A, 583, A57
Stein, R. F., & Nordlund, Å. 1998, ApJ, 499, 914
Suess, H. E., & Urey, H. C. 1956, Rev. Mod. Phys., 28, 53
Summers, H. P., & O'Mullane, M. G. 2011, AIP Conf. Ser., 1344, 179
Tachiev, G., & Froese Fischer, C. 1999, J. Phys. B At. Mol. Phys., 32, 5805
Takeda, Y. 2022, Sol. Phys., 297, 4
Takeda, Y., Tajitsu, A., Honda, S., et al. 2011, PASJ, 63, 697
Unsöld, A. 1955, Physik der Sternatmospharen, MIT besonderer Berucksichtigung der Sonne (Berlin Heidelberg: Springer-Verlag)
van Regemorter, H. 1962, ApJ, 136, 906
Wang, E. X., Nordlander, T., Asplund, M., et al. 2021, MNRAS, 500, 2159
Wood, B. J., Smythe, D. J., & Harrison, T. 2019, Am. Mineral., 104, 844
Yakovleva, S. A., Voronov, Y. V., & Belyaev, A. K. 2016, A&A, 593, A27
Zatsarinny, O. 2006, Comput. Phys. Commun., 174, 273
Zhou, Y., Amarsi, A. M., Aguirre Børsen-Koch, V., et al. 2023, A&A, 677, A98